Nickel quantum dots anchored in bio-derived nitrogen-doped carbon as bifunctional electrocatalysts for overall water splitting

Abstract

Quantum dots (QD) gained increasing interest in the last few years as electrocatalysts due to their outstanding properties, such as excellent catalytic activity and good thermodynamic stabilities. Mixing them with carbon materials enhances their performance and addresses some of the problems associated with their low conductivity. However, most QD-carbon hybrids show catalytic activities way less than that theoretically predicted due to the aggregation of the QD or the QD-carbon nanostructures during processing. Herein, we introduce a universal concept for preparing QD-carbon nanostructures that show almost no aggregation during the materials synthesis, electrode fabrication or even during operation as electrocatalyst for overall water splitting. The new concept is based on using biomass as a source of carbon. The cells walls and membranes in the biomass raw materials are usually rich in sites that attract metal ions from surrounding atmospheres. We used these sites to regulate the deposition and growth of Ni from a salt precursor by a simple solution impregnation method. Due to the abundance of the seeding sits and the limited supply of Ni^{+}, the Ni particles growth is restricted to the QD level with 3-4 nm sizes. The formed Ni compounds QD are strongly linked to the cells walls and membranes, which could be maintained after subsequent heat treatment. The prepared 3D architecture (Ni@C-N), has high catalytic activity, large surface area, strong physical integration, and rapid charge transfer capability, which collectively enhances the performance toward OER and HER. Our DFT calculations proved the binding and dissociation energies between the surface of the Ni@C-N and the water-splitting intermediates; H_2O, H, and OH match that of the expensive noble metal-based electrocatalysts. With the possibility of using a similar approach to design other bifunctional catalysts, the present work opens the door to empower the next generation green fuel conversion for carbon neutral.

Keywords: Nickel nanocrystals; N-doped carbon; Bifunctional electrocatalysts; Overall water splitting; DFT

1. Introduction

Hydrogen is considered a promising clean energy carrier to satisfy the growing energy demands and fulfil the goal of reducing carbon emissions.[1-3] As an alternative to grey hydrogen, where hydrogen is produced by cracking hydrocarbon gases at high temperatures, green hydrogen is produced by the electrolysis of water in what is known as water splitting. [4-6] In the electrochemical water splitting, hydrogen is produced at the cathodic through hydrogen evolution reaction (HER), and anodic oxygen evolution reaction (OER) produces pure oxygen.[7-10] The process requires the use of efficient electrocatalysts, such as the Pt HER catalyst, the IrO_2 and RuO_2 OER catalysts. [11-16] Despite development in producing and enhancing the performance of these noble metals or rare earth compounds, the majority of the water-splitting cost is still the cost of electrocatalysts. [17, 18] [19-21] It is important to develop efficient non-precious metals bifunctional electrocatalysts for HER and OER in the same electrolyte.[22, 23]

As an alternative to the expensive noble and rare earth metals, the transition metal compounds have been used successfully in recent years. Metallic Ni, Co, Fe, and their oxides, chalcogenides, carbides, selenides, and phosphides, have garnered particular attention due to their good electrocatalytic performances for HER and OER, which is comparable to that of Pt-based catalysts. [27-33] However, most transition metal-based compounds have relatively low electrical conductivity, limiting the charge transfer and weakens their electrocatalytic activity. A common concept to improve the conductivity is by mixing or coating the transition metal compounds with carbon nanomaterials to form conductive electrocatalysts.[24-26] These composite electrocatalysts are intensively studied yet show high overpotential and poor stability for HER and OER.[34, 35] It is commonly believed that the catalytic activity is originated from moderate bonding energy between the proton and hydride acceptor sites on the surface of the electrocatalyst and the reaction intermediates in water splitting. Nevertheless, the metallic nanocatalysts tend to form agglomerates or polydisperse of varying sizes regardless of the synthesis methods due to their high surface energy.[36-38] This covers a significant part of the electrocatalyst surface and changes the bonding energy with the intermediates, reducing or even passivating the catalytic activities. Also, the particle aggregation during the electrode fabricating weakens the contact between catalysts and substrates and might lead to peeling the metal catalysts during the water splitting.[42-44] The unstable electrode might also suppress the catalytic reaction on the catalyst surface owing to the tough electron

penetration, further limiting their applications.[38-41] Therefore, despite the reported significant progress, it is important to develop efficient transition metal catalysts strongly immobilized on carbon matrix through a simple, controllable, and scalable synthesis method.

Herein, we present a concept to fabricate Ni QD anchored on 3D honeycomb-like N-doped carbon (Ni@C-N) bifunctional nanocatalysts through a simple solution impregnation followed by an annealing step. The N-doped carbon (C-N) works mainly as a backbone to support the Ni QD but also provides the nanocatalysts with good electrical conductivity, fast charge transport, unique 3D morphology with a high surface area. Due to the confinement effect originated from the strong chemical bonding between the Ni ions and cell wall or membrane in biomass raw materials, the as-prepared Ni nanocrystals are restricted to the QD size of about 3-4 nm, much smaller than that reported in the literature for Ni-carbon composites. The synergy between the catalytically active QD and the multifunction N-C backbones provides Ni@C-N with a unique set of properties that promotes efficient electrocatalytic processes. Furthermore, the strong chemical bond between the Ni QD and the C-N support facilitates the charge transfer and provides good long-term stability. Besides, this new method is also simple, controllable, low-cost, and environmentally friendly. Thus, the new concept offers a promising strategy for fabricating various non-noble metal electrocatalysts in fuel cells, energy storage, chemical industry, petrochemical, biochemical, environmental protection fields.

2. Materials and experimental method

Chemicals and raw materials. The biomass materials, including asparagus (AG), white radish (WR), and potato (PT), were purchased from the supermarket. $Ni(NO_3)_2 \cdot 6H_2O$, KOH, and Milli-Q ultrapure water (Millipore, ≥ 18.2 MΩ· cm) were purchased from Shanghai DeNA. The Nafion solution (5 wt%, D520), deionized water and absolute ethanol were purchased from Shanghai Hesen. All chemical reagents were of analytical grade.

Synthesis of Ni@C-N nano-catalysts. The biomass materials were cut into small cubes and impregnated with $Ni(NO_3)_2 \cdot 6H_2O$ aqueous solutions with different concentrations (0.1, 0.2, 0.3, 0.4, and 0.5 M) for 2 h. To maintain the biochar materials' morphological integrity and ionic dispersion, all the macerated samples were placed in a freeze dryer to obtain the composite precursors. After freeze-drying, the as-obtained precursors were further annealed at different temperatures (400, 500, 600, 700, 800, and 900 °C) in Ar atmosphere for 2 h with a heating rate of 2 °C/min. Different

samples were prepared using a similar method, and the abbreviations of these materials were listed in Table S1.

Characterization. The powder X-ray diffraction (XRD) patterns were recorded at room temperature by a diffractometer (AXS D8 Advance, Bruker) equipped with a Cu Kα radiation. The morphology and composition of the prepared catalysts were characterized by scanning electron microscopy (SEM, JSM-7001F, JEOL) equipped with an energy dispersive spectroscopy (EDS) microanalyzer (QUANTAX EDS, Bruker). The structure and morphology of the as-prepared composite nanoparticles were further studied by transmission electron microscopy (TEM, Tecnai G2 F30 S-TWIN, FEI), high-resolution transmission electron microscope (HRTEM), and selected area electron diffraction (SAED). Nano Measurer calculated the size distribution of Ni nanoparticles. Raman spectroscopies (HORIBA LabRAM HR Evolution instrument) were carried out under the excitation at 532 nm. X-ray photoelectron spectroscopy (XPS) data was collected via an X-ray photoelectron spectrometer (ESCALAB 250XI, Thermo). Inductively coupled plasma optical emission spectroscopy (ICP-OES) was performed on an Agilent 5110 instrument. The Brunauer-Emmett-Teller (BET) surface areas of the prepared materials were measured on an ASAP 2020 physisorption analyzer (Micromeritics Instrument Corporation).

Electrochemical tests. The electrochemical measurements, e.g. linear sweep voltammetry (LSV), were carried out on a three-electrode system in 1.0 M KOH at 25 °C, connecting with an electrochemical workstation (CHI660E). A Pt slice was used as a counter electrode, while an Ag/AgCl electrode with saturated KCl and a glassy carbon electrode (GCE) were selected as the reference and working electrodes, respectively. All potentials *vs* Ag/AgCl reported herein were converted to the reversible hydrogen electrode (RHE) with the Nernst equation ($E_{RHE} = E_{Ag/AgCl} + 0.059\ pH + 0.197$). All polarization curves were IR-corrected with 90% IR compensation. The overpotential for OER is calculated by $\eta(V) = E_{RHE} - 1.23$ V. The catalytic dispersions or inks were prepared by mixing 5 mg catalyst in a 1 mL solution mixture containing 750 μL of ethanol, 200 μL of ultrapure water (DeNA), and 50 μL of the Nafion solution (5 wt%, D520). The mixture was sonicated for at least 30 min to form a homogeneous solution and deposited on a freshly polished GCE (diameter = 5 mm).

Density functional theory calculation. Based on the density functional theory (DFT), the Vienna ab initio simulation package (VASP) was used in all calculations.[45-47] The exchange-correlation

interactions were applied using the generalized gradient approximation of the Perdew-Burke-Ernzerhof functional (PBE type).[48, 49] The plane-wave cut-off energy was set to 400 eV, and the Brillouin-zone integration was set to a k-mesh of 3×3×3. The energy convergence criterium for atomic structures was 10^{-4} eV/atom, and the convergence threshold for the forces was 0.01 eV/Å. To avoid interactions between neighbouring slices due to lattice periodicity, a vacuum slab of 15 Å was introduced in the z-direction.

3. Results and discussion

Design of the Ni@C-N composite nanocatalysts. A schematic diagram of the synthesis process of Ni@C-N is shown in Fig. 1a. Firstly, the biomass materials, AG, WR, and PT, were impregnated with $Ni(NO_3)_2$ aqueous solution for 2 h, and subsequently freeze-dried to obtain the green precursor. The green precursor was then annealed at 800 ℃ in an Ar atmosphere to obtain the nickel QD supported on N-doped bioderived carbon. For comparison, we also prepared Ni-free N-doped carbon material (C-N-AG) by impregnating the biomass materials in deionized water for 2 h. The synthesis mechanism of Ni@C-N samples can be understood from the structure and composition of plant cells and by taken AG as an example. When the AG is impregnated into the $Ni(NO_3)_2$ solution, Ni^{2+} ions firstly diffuse and penetrate through the cell membrane; then ion exchange occurs between Ni^{2+} ions and cellulose (and phospholipid molecule or membrane protein) in the cell wall or membrane, as shown in Equation S1-S3, respectively. As a result of the ion exchange process, most Ni^{2+} ions are discharged and grow to form Ni-containing nanoparticles bonded to the cells surface of the cell wall and membrane. Following the freeze-drying desiccation process, the honeycomb structure of natural AG could be maintained, and the Ni-containing nanoparticles are still uniformly deposited on the cell wall and membrane. The carbon from the biomass source reduces Ni-containing nanoparticles into metallic Ni nanoparticles (or QD) during the annealing step. In the meantime, N and C from the biomass raw materials react to form the C-N backbone supports. The annealing process doesn't harm the original bond between Ni^{2+} ions and the cell wall, meaning stable chemical bonds are exist between the formed Ni nanoparticles and C-N. Since there are numerous active sits for the Ni^{2+} ions deposition, the number of ions available per sit is limited, which also controls the particles' growth. The uniform distribution of the active growth sits also satisfies the Ni particles' homogeneous distribution and prevents their aggregation. This suggested mechanism finds some supporting evidence from the structural and chemical analysis of the produced composite, as

discussed in the following paragraphs.

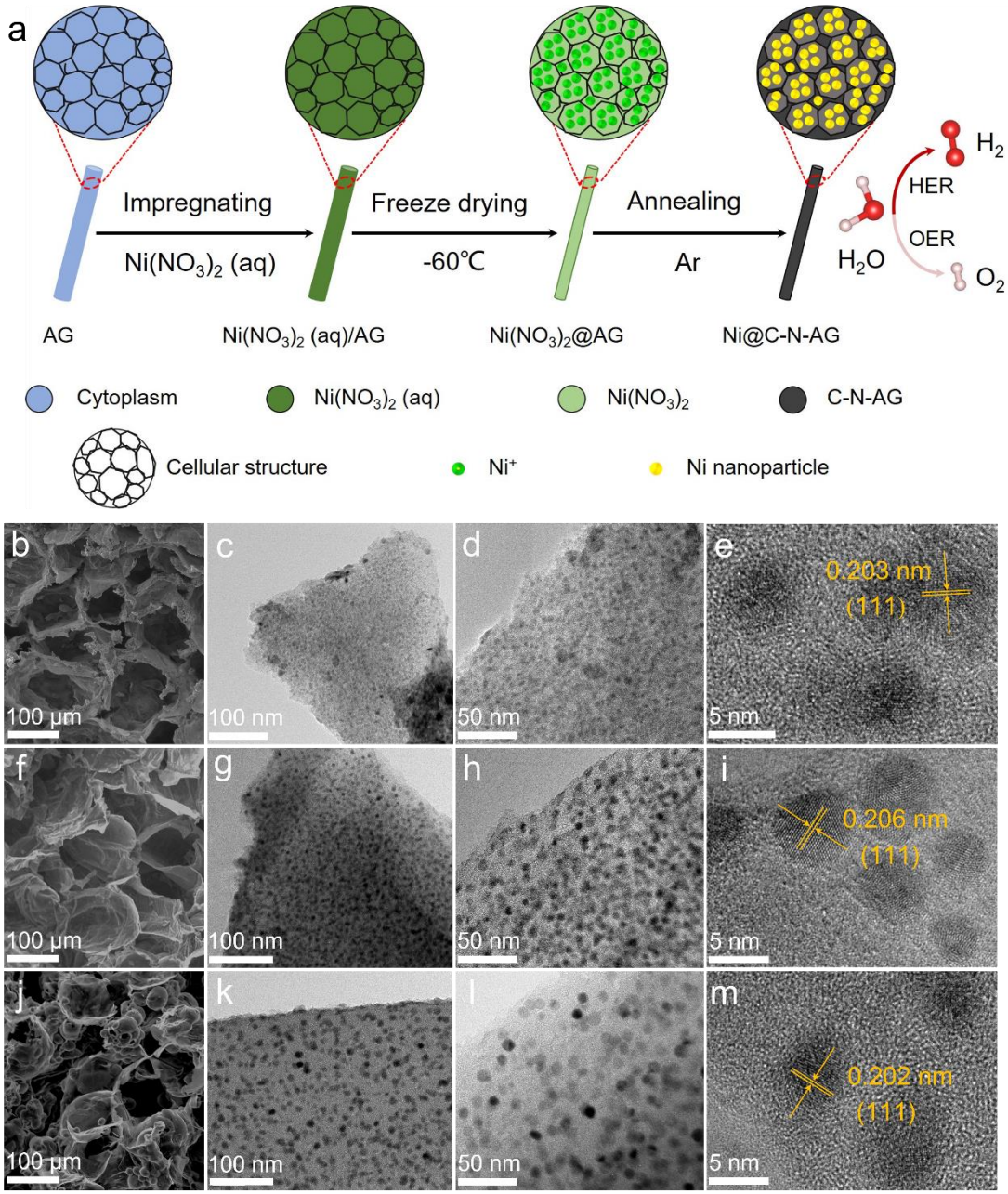

Fig. 1. (a) Schematic diagram for the preparation process of Ni@C-N nanocomposites, using the biomass material AG as an example. (b-m) The morphology of Ni@C-N nano-electrocatalysts. SEM images of Ni@C-N-AG (b), Ni@C-N-WR (f), and Ni@C-N-PT (j); TEM images in different magnifications of Ni@C-N-AG (c, d), Ni@C-N-WR (g, h), and Ni@C-N-PT (k, l); HRTEM images of Ni@C-N-AG (e), Ni@C-N-WR (i), and Ni@C-N-PT (m).

Despite the different biomass sources, all the produced materials showed almost the same honeycomb for the carbon backbone (Fig. 1b, f, j, Fig. S1). This unique 3D architecture is composed

of very thin connected carbon walls, giving a high specific surface area of 233.3 m^2/g after annealing (Fig. S2, Table S2). The pyrolysis of the hydrocarbon and the volatile materials' release during the annealing produce macropores and micropores of different sizes. The magnified TEM and HRTEM detected quantum dots of the size 3-7 nm uniformly distributed on the surface of C-N layers, with almost no aggregation or agglomeration (Fig. 1c, g, k). The interlayer distance measured from lattice fringes in figure 1e, i and m are about 0.203 nm, typical for the (111) plane of metallic Ni. The Ni nanocatalysts SAED patterns (Fig. S5) are also in line with the HRTEM results. The XRD analysis also confirms the crystallinity of the Ni particles, with diffraction peaks at 44.5, 52.0, and 76.2° corresponds to the (111), (200) and (220) lattice planes of cubic-structured Ni (Figures 2a and S7). Interestingly, the particle size of the formed Ni QD differs with respect to the type of biomass raw materials, suggesting the composition and structure of the biomass might play an important role in the growth of the Ni QD. Nevertheless, the size of Ni nanoparticles in Ni@C-N-AG composite is much smaller than reported literature (about 7−50 nm), which is critical for the exposure of active catalytic sites.[50] The EDS analysis further confirms the uniform distribution of Ni QD alongside other elements such as N, O, and C. The graphitization of the N-doped carbon backbone of the composite is first confirmed by the XRD, where a broad diffraction peak can be observed at 26.4° in the pattern of the C-N-AG controlled samples. The Raman spectroscopic analysis further confirms the graphitization. The peak that appears at 1580 cm^{-1} (G band) in all samples spectra is attributed to the graphitic sp^2 carbon (E_{2g}). The other peaks in the spectra are; the D1 at around 1350 band for the disordered sp^3 carbon defects (A_{1g}), the D3 band for amorphous carbon, and the D4 band for the polyene-like carbon structures or ionic impurities. [51] The intensity ratio of the D1 and G bands (I_{D1}/I_G) decreases with the increasing temperature (Fig. S9, Table S3), suggesting the enhancing graphitic structure of the C-N matrix at high temperature. The strong bonding between Ni QD and the N-doped carbon backbones is first confirmed extensive sonication for 1 h. No apparent changes are observed after sonication, as shown by the SEM images in Fig. S6. The strong adhesion between Ni QD and C-N is beneficial for the electron transfer capability and the long-term electrocatalytic stability.

Moreover, the XPS was performed to analyze the surface element composition and valence states in the Ni@C-N-AG composite. The survey XPS spectrum reveals the presence of Ni, C, N, and O elements (Fig. S10) with no obvious impurity, consistent with the EDX and XRD results. In the

high-resolution Ni 2p spectrum, as shown in Fig. 2c, the peaks at 853.0 and 870.2 eV are ascribed to Ni^0 species from the Ni-Ni metallic bond in Ni nanoparticles.[52] The peaks at 855.7 and 873.4 eV correspond to the oxidized Ni species,[53] most likely formed by the surface oxidation of Ni QD. The absence of any signs for Ni-O compounds in the XRD patterns suggested the oxidation is limited to the QD surface. Detecting different Ni valences in the same nanoparticles suggests different functional groups and stoichiometry of Ni-O, which is beneficial for the electrocatalytic HER performance.[30, 54] The deconvoluted high-resolution spectrum of C 1s spectrum reveals peaks for the C-C (284.7 eV), C-N (285.4 eV), and C-O-Ni (288.6 eV) species (Fig. 2d).[55] Detecting the peak at 288.6 eV C-O-Ni provide evidence that the interactions between Ni QD and the N-doped carbon go beyond the weak physical attachments to a strong chemical bond, which is beneficial for long cycle life. The N 1s spectrum is deconvoluted into three characteristic peaks at 398.8, 400.8 and 401.4 eV, which are attributed to pyridinic N, pyrrolic N, and graphitic N, respectively (Fig. 2e).[40] The high-resolution XPS spectra of C 1s and N 1s further confirm the incorporation of nitrogen element in the carbon matrix,[57] which could also facilitate the bonding between the Ni nanoparticles and the C-N layer. Our DFT calculation (Fig. S11) suggested the pyridinic N is preferential to link N with the Ni, forming highly active Ni-N sites for various electrocatalysis processes.[56] The content of N is quantitatively calculated to be about 0.23 at%, and the atomic ratio of Ni:C in the Ni@C-N-AG sample is found to be 3.38:1 (Table S4), which is well consistent with Ni loading amount of 42.6 wt% measured by ICP-OES.

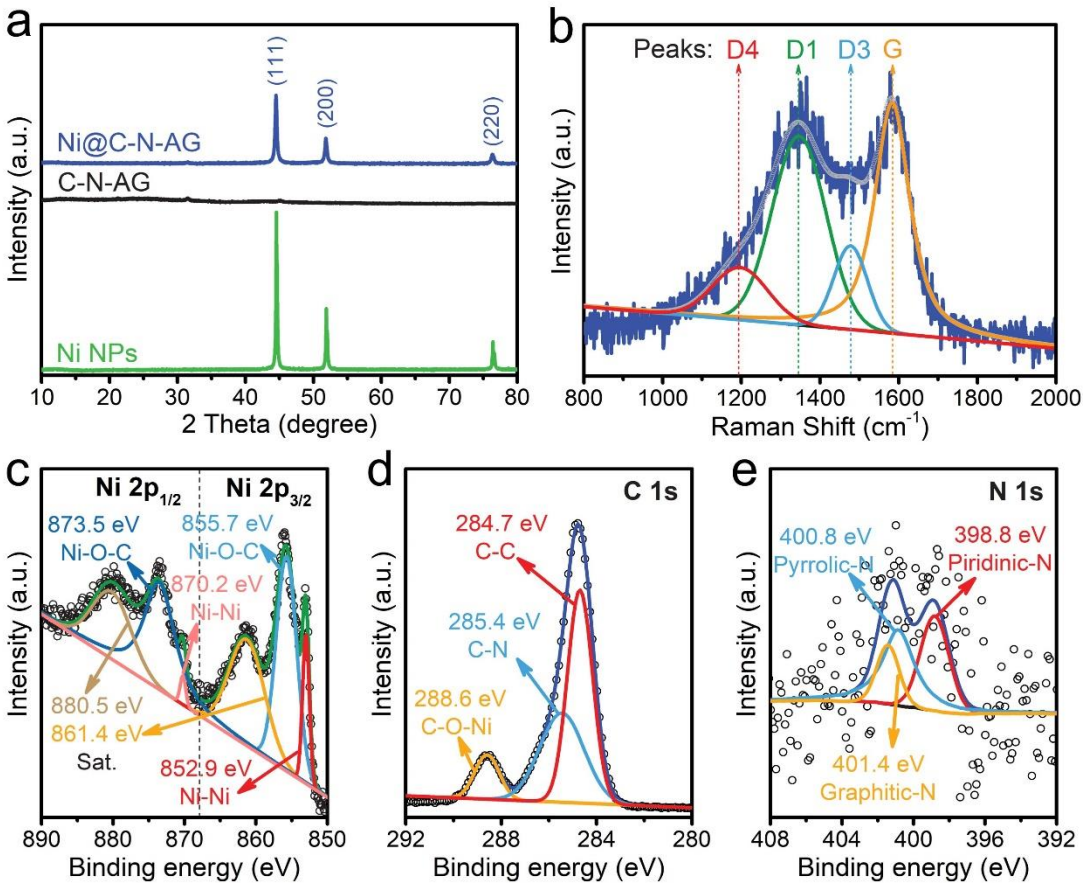

Fig. 2. The structure of Ni@C-N-AG nano-electrocatalysts. (a) XRD patterns of Ni@C-N-AG, C-N-AG, Ni nanoparticles (Ni NPs); (b) Curve fitting of the Raman spectrum of Ni@C-N-AG; (c-e) High-resolution XPS spectra of Ni 2p (c), C 1s (d), and N 1s (e) of Ni@C-N-AG. It should be noted that the Ni $2p_{3/2}$ band shows peaks at 852.9 and 855.7 eV along with one shakeup satellite peak at 861.4 eV, while the Ni $2p_{1/2}$ spectrum exhibits two peaks at 870.2 and 873.5 eV with a satellite peak at 880.5 eV.

Electrochemical performances. The HER and OER activities were investigated via a three-electrode system in 1.0 M KOH solution. Firstly, the HER performances as the functions of immersion solution concentration and annealing temperature were evaluated. The best HER activity is obtained at the $Ni(NO_3)_2$ solution concentration of 0.3 M and the annealing temperature of 800 °C (Fig. S12, S13, and Table S5), suggesting these conditions are optimum to synthesis efficient structures for electrocatalysts. Furthermore, various loading of the active materials ranged from 0.2 to 1.25 mg/cm^2 were cast on the glassy carbon current collector. The optimum loading was found to be 1.25 mg/cm^2 (Fig. S14, Table S6), and hence the electrodes used for the rest of the electrochemical investigation are all fabricated and tested at these conditions. For comparison, we

also investigate other electrodes' catalytic performance, including commercial 20 wt% Pt/C, Ni NPs, and C-N-AG for HER, as shown in Fig. 3a. Commercial Pt/C catalyst exhibits the highest activities for HER with an overpotential of 27 mV at the current density of 10 $mA \cdot cm^{-2}$, way less than the overpotential of both the Ni-free C-N-AG and commercial Ni NPs. By anchoring the Ni QD on the C-N-AG backbone, the as-prepared Ni@C-N-AG exhibits high HER activity with a low onset potential of 86 mV.[42, 58] Only 170 mV is needed to achieve a current density of 10 $mA \cdot cm^{-2}$ for Ni@C-N-AG, and the overpotentials to produce current densities of 50, 100, and 180 $mA \cdot cm^{-2}$ are 280, 360, and 430 mV, respectively. These results indicated the synergy between Ni QD and the N-doped carbon porous backbone facilities the catalytic process with overpotentials in KOH alkaline electrolyte lower or comparable with the most active Ni-based and non-noble based catalysts.[43, 59] Under the same condition, the initial overpotential recorded for the Ni@C-N-AG electrode is lower than any reported bio-derived C-N composite reported in the literature (Fig. 3b, Table S7).[16, 60-62] The Tafel slope of Ni@C-N-AG is 68 mV dec^{-1}, which is close to that of the commercial Pt/C (41 mV dec^{-1}), and far below the Ni NPs (190 mV dec^{-1}) (Fig. 3c, Table S8). This result indicates that the HER process occurs through a Volmer-Heyrovsky mechanism, which signifies rate-limiting electrochemical recombination with an additional proton after a fast discharge of a proton. The relatively small Tafel slop for Ni@C-N is also satisfying to acquire a sizeable current density at low overpotential, confirming that high activity toward HER. It is suggested that the increased activity is ascribed to the large specific surface area and the availability of numerous sites for electrocatalysis. Besides, the graphitized 3D C-N matrix promotes the charge transfer in the Ni@C-N catalyst, further enhances the overall HER activity.

The electrochemical stability of Ni@C-N-AG is investigating by a long-term chronoamperometry method in a 1.0 M KOH solution. After 10 h of electrolysis at a constant potential of −207 mV, no significant current decay can be observed (Fig. 3d). Furthermore, the polarization curve shifts negligibly at a higher current density of 175 mA cm^{-2} (Fig. 3e), suggesting good electrochemical stability for HER catalysis in alkaline solution. The TEM image of the sample after the long-term HER process shows almost no changes in the original structure of Ni@C-N, confirming the excellent stability of the prepared composite as a result of the strong bonds between Ni QD and the C-N backbone (Fig. S15).

We then evaluated the catalytic activity of Ni@C-N-AG toward OER in the same setup with 1.0

M KOH electrolyte. Electrodes fabricated using commercial IrO_2/C, Ni NPs, and C-N-AG are also examined for comparison. As shown in Fig. 3f, without Ni QD, the C-N-AG network exhibits nearly no OER activity. Commercial IrO_2/C offers the best OER performance when the produced current density is higher than 10 $mA \cdot cm^{-2}$. However, at a current density lower than 10 $mA \cdot cm^{-2}$, Ni@C-N-AG perform better than other tested electrodes with the lowest overpotential of 319 mV. The overpotentials of 353, 400, 492 mV are required to yield the current density 20, 50, and 100 $mA \cdot cm^{-2}$, comparable with that required by the IrO_2/C and outperformed other Ni/Carbon composites in the literature (Table. S8, S9). The Tafel slope of Ni@C-N-AG is calculated to be 93 mV dec^{-1}, which is closed to the commercial IrO_2/C and much lower than Ni NPs (Fig. 3g, Table S8), indicating a fast OER catalytic kinetic for Ni@C-N-AG. Finally, the HER and OER activities of Ni@C-N-AG are compared with those of some state-of-the-art non-noble metal-based bifunctional electrocatalysts, as shown in Table S10. The HER and OER performances of Ni@C-N-AG catalyst at 10 $mA \cdot cm^{-2}$ are comparable to those of other bifunctional electrocatalysts in alkaline media. The high catalytic activities, long-life stability coupling with the cheap and sustainable precursor, make the Ni@C-N electrodes excellent candidates for practical application for water splitting.[63]

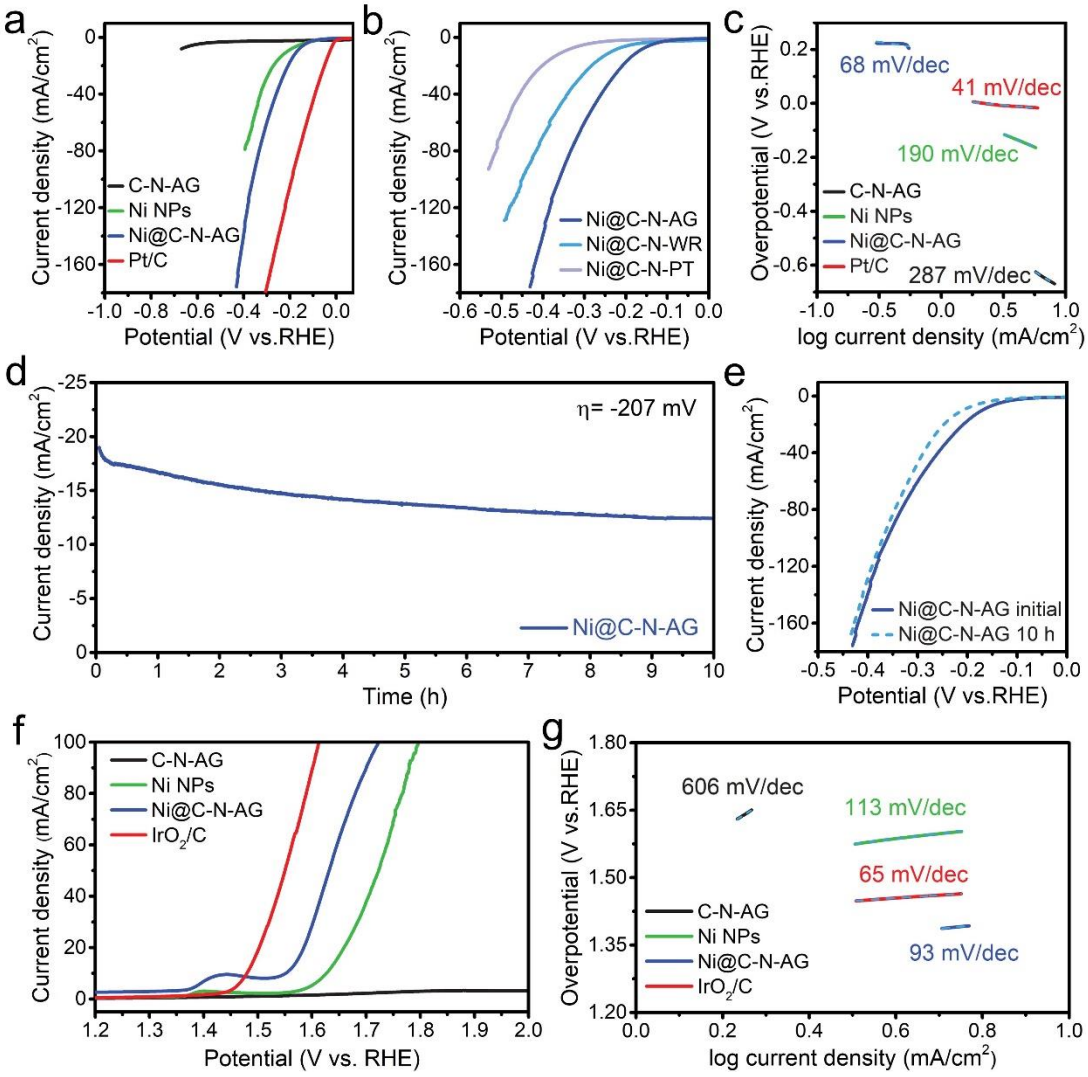

Fig. 3. Electrochemical performance of Ni@C-N-AG in 1.0 M KOH solution. (a) HER polarization curves of C-N-AG, Ni NPs, Ni@C-N-AG, and Pt/C; (b) HER polarization curve of Ni@C-N-AG, Ni@C-N-WR, and Ni@C-N-PT; (c) Tafel plots obtained from the linear sweep voltammetry (LSV) polarization curves in (a); (d) Chronoamperometric curve of Ni@C-N-AG at the overpotential of − 207 mV for 10 h; (e) LSV curves of Ni@C-N-AG before and after 10 h of chronoamperometry; (f) OER polarization curves of C-N-AG, Ni NPs, Ni@C-N-AG, and IrO_2/C. (g) Tafel plots for the OER LSV curves in (f).

DFT calculations. The overall water splitting reaction mechanism in alkaline solutions are proposed in Fig. 4a and Fig. S16, in which the OER process involves four steps, namely, OH^-, OH_{ads}, O_{ads} and OOH_{ads}. [64] The HER consists of electrochemical hydrogen adsorption (Volmer reaction) and chemical desorption (Tafel reaction).[65] The specific reaction pathway includes H_2O adsorption, the electrochemical dissociation of adsorbed H_2O into adsorbed OH^- and H^+, the OH^- desorption to

refresh the surface, and the H_2 formation.[66] First-principles DFT calculations could shade more light on the HER activity of Ni@C-N in the alkaline solution and the role of the active sites. The binding energies of H_2O, H^+ and OH^-, as well as H_2O dissociation on the Ni_{13}@C-N, Pt_{13}, Ni_{13}, and C-N surfaces were explored (Fig. 4b-e, Fig. S17-S19). First, the M-H_2O binding energy of Ni_{13} is close to that of Pt_{13}, but both are much higher than that of C-N. When the Ni_{13} nanoparticles are anchored on C-N, the M-H_2O binding energy increases significantly (Fig. 4f, Fig. S17), accelerating the adsorption of H_2O and pushing the Volmer reaction toward the right side. Also, H_2O dissociation on Ni_{13}@C-N surface is comparable to Pt_{13}, which is much lower than that on Ni_{13} and C-N surfaces (Fig. 4b-e). These results indicate the dissociation of H_2O into H^+ and OH^- on Ni_{13}@C-N surface is fast, promoting a fast proton source supply for the HER. After dissociation, our DFT calculation shows that the M-H^+ binding energy with Ni_{13}@C-N is slightly lower than the ideal HER candidate Pt_{13} (Fig. 4g, Fig. S18), and the OH^- binding energy is slightly higher (Fig. 4h, Fig. S19). The moderate H^+ and OH^- binding energies could expedite the creation of M-H^+ and simultaneously refresh the active site on the Ni_{13}@C-N surface, improving the HER efficiency in alkaline solutions. This calculated mechanism is perfectly in line with our experimental results. It demonstrates that the strategy by anchoring Ni QD on C-N support can significantly improve the efficiency and kinetic of HER electrocatalytic to a level close to that of the expensive noble metal catalyst.

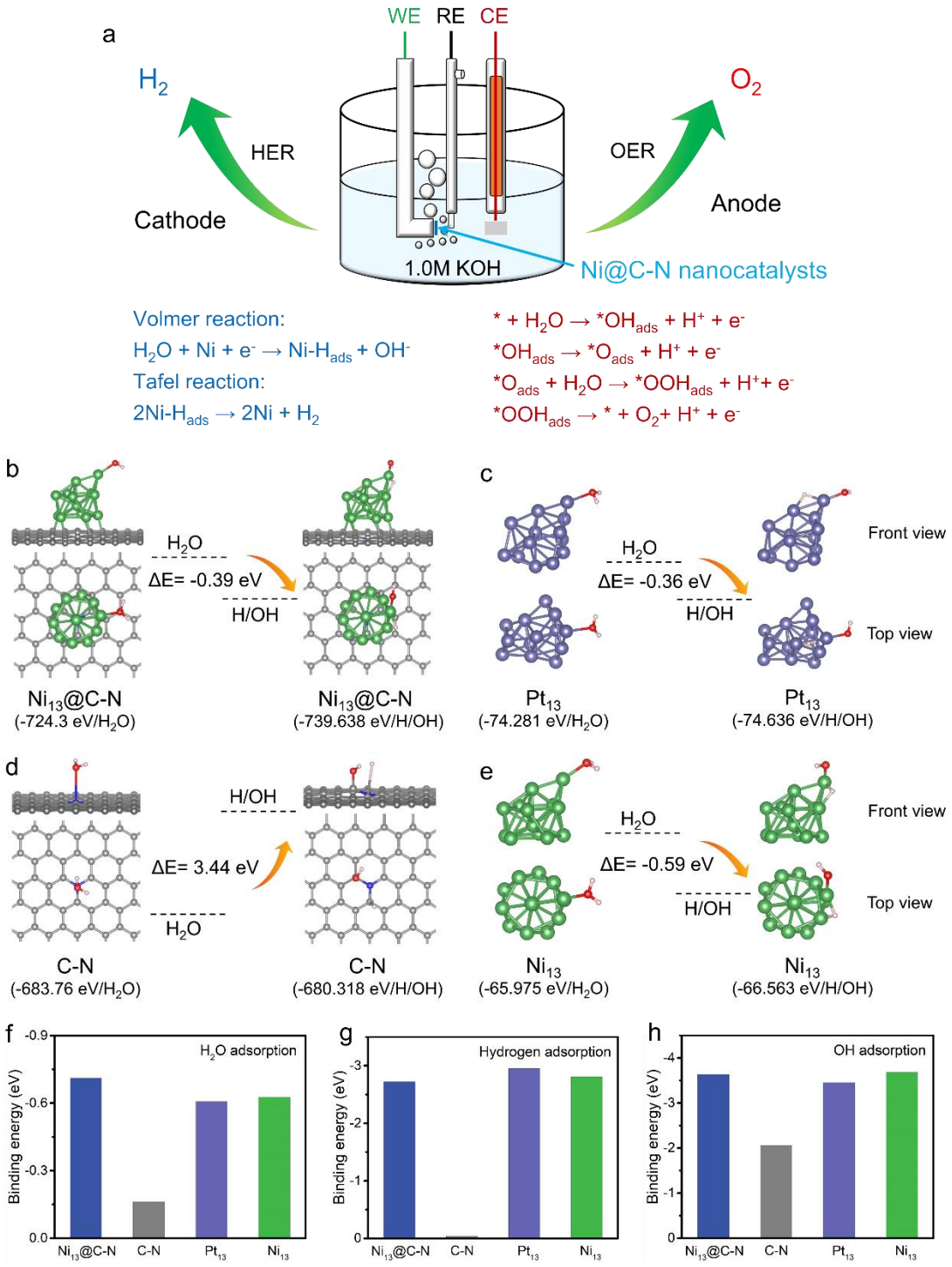

Fig. 4. Detail water splitting reactions (a) and DFT calculations (b-h) for HER reactivity of in alkaline solution. (a-d) Adsorbed H_2O dissociation configuration on the surfaces: (b) Ni_{13}@C-N, (c) C-N, (d) Pt_{13} nanoparticles, (e) Ni_{13} nanoparticles, as well as their binding energies in alkaline solution. The green, grey, blue, purple, red, and ivory balls represent Ni, C, N, Pt, O, and H atoms, respectively. (f-h) H_2O binding energies (f), H binding energies (g), OH binding energies (h) on the different surfaces of Ni_{13}@C-N, C-N, Pt_{13} nanoparticles, and Ni_{13} nanoparticles in alkaline solution.

The mechanism of Ni@C-N nanocatalyst for HER and ORR can be further discussed. The graphitized 3D C-N in the composite ply triple roles; (a) the network provides a high surface area to interact with electrolyte, (b) it provides the active sites required for the deposition and growth of Ni QD without aggregation or exfoliation, and (c) it promotes the interelectron transport along with the interface of Ni@C-N between Ni nanocrystals and C-N. The Ni@C-N heterojunction with a tight connection between Ni nanocrystal and C-N offers a unique host-guest electronic interaction, which results in an electrically conductive path for fast electron transfer. The high catalytic activities can be attributed to the well-exposed active (111) crystal planes with comparable H_2O dissociation energy to Pt catalyst and appropriate binding energies with H_2O, H, and OH for Ni nanocrystal. Furthermore, the distance distribution of the Ni QD on the C-N support can allow the convection and release of H_2 and O_2 bubbles, reducing the damage of the catalysts by the high-pressure gas and facilitate the gases recovery. In general, the Ni@C-N electrocatalyst could gain high HER and OER activities and stable long-term cycling capability thanks to the well-controlled synthesis method that took advantage of the naturally available deposition sits on life cells walls to regulate the growth of Ni QD and prevent their aggregation.

4. Conclusions

This work introduced Ni QD anchored on N-doped carbon derived from various biological sources as a bifunctional catalyst for HER and OER in water splitting. The prepared composite benefited from the abundant active sites on the cell walls and membranes in plants cell to homogeneously deposited Ni+ and consequently discharge it to Ni. By controlling the amount of the Ni precursor, the growth of Ni particles was limited to give QD. The distance between the initial Ni seed sits prevented the Ni QD from aggregation and/or agglomeration. When the green Ni-biomass precursor was heat-treated at 800 oC, the biomass was converted to 3D porous graphitized carbon doped with nitrogen while the Ni compound was reduced to metallic Ni QD (about 3-4 nm in size). The heat treatment also helped to strengthen the bond between Ni QD and the N-doped carbon substrate. The well-designed composite wetted well with water and has a high surface area with enormous catalytically active sites and rapid charge transfer capability. As a result, the Ni@C-N-AG composite exhibits excellent stability and HER and OER activity in 1.0 M KOH alkaline electrolyte. The Ni@C-N-AG needed 170 and 319 mV overpotentials to reach the current density of 10 $mA \cdot cm^{-2}$ for HER and OER, respectively, comparable with the expensive noble metal-based bifunctional

electrocatalysts. The DFT calculation investigated the HER mechanism, which suggested that the well-exposed active (111) crystal planes pf Ni QD have dissociation energy for H_2O very close to that of Pt catalyst. The DFT calculations also proved that the binding energies between Ni QD surface and H_2O, H, and OH are also close to that reported for Pt electrode. We believe that the design of the hybrid electrocatalysts is universal and could be used to synthesis similar QD-carbon as stable bifunctional electrocatalysts for water splitting and other electrocatalysis reactions.

Conflicts of Interest

The authors declare no conflict of interest.

Acknowledgements

This work was financially supported by the National Natural Science Foundation of China (No. 51702293), the Engineering Research Center of Non-metallic Minerals of Zhejiang Province (No. ZD2020K04), and the Fundamental Research Funds for the Central Universities (No. 2652019164, No. 2652019033).

Additional information

Supplementary information is available in the online version of the paper.

References

[1] Han, N.;Liu, P.;Jiang, J.;Ai, L.;Shao, Z.; Liu, S. Recent advances in nanostructured metal nitrides for water splitting. *Journal of Materials Chemistry A* **2018**, *6*, 19912-19933.

[2] Gupta, U.; Rao, C. Hydrogen generation by water splitting using MoS2 and other transition metal dichalcogenides. *Nano Energy* **2017**, *41*, 49-65.

[3] Du, X.;Huang, J.;Zhang, J.;Yan, Y.;Wu, C.;Hu, Y.;Yan, C.;Lei, T.;Chen, W.; Fan, C. Modulating electronic structures of inorganic nanomaterials for efficient electrocatalytic water splitting. *Angewandte Chemie International Edition* **2019**, *58*, 4484-4502.

[4] Roger, I.;Shipman, M. A.; Symes, M. D. Earth-abundant catalysts for electrochemical and photoelectrochemical water splitting. *Nature Reviews Chemistry* **2017**, *1*, 1-13.

[5] Hu, Q.;Li, G.;Li, G.;Liu, X.;Zhu, B.;Chai, X.;Zhang, Q.;Liu, J.; He, C. Trifunctional Electrocatalysis on Dual-Doped Graphene Nanorings–Integrated Boxes for Efficient Water Splitting and Zn–Air Batteries. *Advanced Energy Materials* **2019**, *9*, 1803867.

[6] Zhu, Y. P.;Guo, C.;Zheng, Y.; Qiao, S.-Z. Surface and interface engineering of noble-metal-free

electrocatalysts for efficient energy conversion processes. *Accounts of chemical research* **2017**, *50*, 915-923.

[7] Wu, R.;Xiao, B.;Gao, Q.;Zheng, Y. R.;Zheng, X. S.;Zhu, J. F.;Gao, M. R.; Yu, S. H. A Janus Nickel Cobalt Phosphide Catalyst for High-Efficiency Neutral-pH Water Splitting. *Angewandte Chemie* **2018**, *130*, 15671-15675.

[8] Jiao, Y.;Zheng, Y.;Jaroniec, M.; Qiao, S. Z. Design of electrocatalysts for oxygen-and hydrogen-involving energy conversion reactions. *Chemical Society Reviews* **2015**, *44*, 2060-2086.

[9] Cai, Z.;Bu, X.;Wang, P.;Ho, J. C.;Yang, J.; Wang, X. Recent advances in layered double hydroxide electrocatalysts for the oxygen evolution reaction. *Journal of Materials Chemistry A* **2019**, *7*, 5069-5089.

[10] Zhou, H.;Yu, F.;Sun, J.;He, R.;Chen, S.;Chu, C.-W.; Ren, Z. Highly active catalyst derived from a 3D foam of Fe (PO3) 2/Ni2P for extremely efficient water oxidation. *Proceedings of the National Academy of Sciences* **2017**, *114*, 5607-5611.

[11] Wang, J.;Xu, F.;Jin, H.;Chen, Y.; Wang, Y. Non-Noble Metal-based Carbon Composites in Hydrogen Evolution Reaction: Fundamentals to Applications. *Advanced Materials* **2017**, *29*.

[12] Zou, X.; Zhang, Y. Noble metal-free hydrogen evolution catalysts for water splitting. *Chemical Society Reviews* **2015**, *44*, 5148-5180.

[13] Lin, S.;Wang, H.;Wu, F.;Wang, Q.;Bai, X.;Zu, D.;Song, J.;Wang, D.;Liu, Z.;Li, Z.;Tao, N.;Huang, K.;Lei, M.;Li, B.; Wu, H. Room-temperature production of silver-nanofiber film for large-area, transparent and flexible surface electromagnetic interference shielding. *npj Flexible Electronics* **2019**, *3*.

[14] Lin, S.;Bai, X.;Wang, H.;Wang, H.;Song, J.;Huang, K.;Wang, C.;Wang, N.;Li, B.;Lei, M.; Wu, H. Roll-to-Roll Production of Transparent Silver-Nanofiber-Network Electrodes for Flexible Electrochromic Smart Windows. *Advanced Materials* **2017**, *29*.

[15] Lin, S.;Wang, H.;Zhang, X.;Wang, D.;Zu, D.;Song, J.;Liu, Z.;Huang, Y.;Huang, K.;Tao, N.;Li, Z.;Bai, X.;Li, B.;Lei, M.;Yu, Z.; Wu, H. Direct spray-coating of highly robust and transparent Ag nanowires for energy saving windows. *Nano Energy* **2019**, *62*, 111-116.

[16] Zhao, Y.;Min, X.;Ding, Z.;Chen, S.;Ai, C.;Liu, Z.;Yang, T.;Wu, X.;Liu, Y. g.;Lin, S.;Huang, Z.;Gao, P.;Wu, H.; Fang, M. Metal-Based Nanocatalysts via a Universal Design on Cellular Structure. *Advanced Science* **2019**, *7*, 1902051.

[17] Hou, Y.;Lohe, M. R.;Zhang, J.;Liu, S.;Zhuang, X.; Feng, X. Vertically oriented cobalt selenide/NiFe layered-double-hydroxide nanosheets supported on exfoliated graphene foil: an efficient 3D electrode for overall water splitting. *Energy & Environmental Science* **2016**, *9*, 478-483.

[18] Raja, D. S.;Lin, H.-W.; Lu, S.-Y. Synergistically well-mixed MOFs grown on nickel foam as highly efficient durable bifunctional electrocatalysts for overall water splitting at high current densities. *Nano Energy* **2019**, *57*, 1-13.

[19] Sun, H.;Li, J.-G.;Lv, L.;Li, Z.;Ao, X.;Xu, C.;Xue, X.;Hong, G.; Wang, C. Engineering hierarchical CoSe/NiFe layered-double-hydroxide nanoarrays as high efficient bifunctional electrocatalyst for overall water splitting. *Journal of Power Sources* **2019**, *425*, 138-146.

[20] Yao, M.;Sun, B.;Wang, N.;Hu, W.; Komarneni, S. Self-generated N-doped anodized stainless steel mesh for an efficient and stable overall water splitting electrocatalyst. *Applied Surface Science* **2019**, *480*, 655-664.

[21] Zhen, W.;Ma, J.; Lu, G. Small-sized Ni(1 1 1) particles in metal-organic frameworks with low over-potential for visible photocatalytic hydrogen generation. *Applied Catalysis B: Environmental* **2016**, *190*, 12-25.

[22] Shi, Y.; Zhang, B. Recent advances in transition metal phosphide nanomaterials: synthesis and applications in hydrogen evolution reaction. *Chem Soc Rev* **2016**, *45*, 1529-1541.

[23] Ledendecker, M.;Calderon, S. K.;Papp, C.;Steinrueck, H.-P.;Antonietti, M.; Shalom, M. The Synthesis of Nanostructured Ni_5P_4 Films and their Use as a Non-Noble Bifunctional Electrocatalyst for Full Water Splitting. *Angewandte Chemie-International Edition* **2015**, *54*, 12361-12365.

[24] Anantharaj, S.;Ede, S. R.;Sakthikumar, K.;Karthick, K.;Mishra, S.; Kundu, S. Recent Trends and Perspectives in Electrochemical Water Splitting with an Emphasis on Sulfide, Selenide, and Phosphide Catalysts of Fe, Co, and Ni: A Review. *Acs Catalysis* **2016**, *6*, 8069-8097.

[25] Liu, X.;Wang, X.;Yuan, X.;Dong, W.; Huang, F. Rational composition and structural design of in situ grown nickel-based electrocatalysts for efficient water electrolysis. *Journal of Materials Chemistry A* **2016**, *4*, 167-172.

[26] Xu, Y.;Tu, W.;Zhang, B.;Yin, S.;Huang, Y.;Kraft, M.; Xu, R. Nickel Nanoparticles Encapsulated in Few-Layer Nitrogen-Doped Graphene Derived from Metal-Organic Frameworks as Efficient

Bifunctional Electrocatalysts for Overall Water Splitting. *Advanced Materials* **2017**, *29*.

[27] He, X.;Luan, S. Z.;Wang, L.;Wang, R. Y.;Du, P.;Xu, Y. Y.;Yang, H. J.;Wang, Y. G.;Huang, K.; Lei, M. Facile loading mesoporous Co_3O_4 on nitrogen doped carbon matrix as an enhanced oxygen electrode catalyst. *Materials Letters* **2019**, *244*, 78-82.

[28] Luo, J.;Im, J.-H.;Mayer, M. T.;Schreier, M.;Nazeeruddin, M. K.;Park, N.-G.;Tilley, S. D.;Fan, H. J.; Grätzel, M. Water photolysis at 12.3% efficiency via perovskite photovoltaics and Earth-abundant catalysts. *Science* **2014**, *345*, 1593-1596.

[29] Wang, H.;Lee, H.-W.;Deng, Y.;Lu, Z.;Hsu, P.-C.;Liu, Y.;Lin, D.; Cui, Y. Bifunctional non-noble metal oxide nanoparticle electrocatalysts through lithium-induced conversion for overall water splitting. *Nature communications* **2015**, *6*, 1-8.

[30] Gong, M.;Zhou, W.;Tsai, M.-C.;Zhou, J.;Guan, M.;Lin, M.-C.;Zhang, B.;Hu, Y.;Wang, D.-Y.; Yang, J. Nanoscale nickel oxide/nickel heterostructures for active hydrogen evolution electrocatalysis. *Nature communications* **2014**, *5*, 1-6.

[31] Yilmaz, G.;Tan, C. F.;Lim, Y. F.; Ho, G. W. Pseudomorphic Transformation of Interpenetrated Prussian Blue Analogs into Defective Nickel Iron Selenides for Enhanced Electrochemical and Photo-Electrochemical Water Splitting. *Advanced Energy Materials* **2019**, *9*, 1802983.

[32] Zhang, D.;Mou, H.;Lu, F.;Song, C.; Wang, D. A novel strategy for 2D/2D NiS/graphene heterostructures as efficient bifunctional electrocatalysts for overall water splitting. *Applied Catalysis B: Environmental* **2019**, *254*, 471-478.

[33] Lv, C.-N.;Zhang, L.;Huang, X.-H.;Zhu, Y.-X.;Zhang, X.;Hu, J.-S.; Lu, S.-Y. Double functionalization of N-doped carbon carved hollow nanocubes with mixed metal phosphides as efficient bifunctional catalysts for electrochemical overall water splitting. *Nano Energy* **2019**, *65*, 103995.

[34] Wang, X.;Yu, L.;Guan, B. Y.;Song, S.; Lou, X. W. Metal–Organic Framework Hybrid-Assisted Formation of Co3O4/Co-Fe Oxide Double-Shelled Nanoboxes for Enhanced Oxygen Evolution. *Advanced Materials* **2018**, *30*, 1801211.

[35] Nai, J.;Zhang, J.; Lou, X. W. D. Construction of single-crystalline Prussian blue analog hollow nanostructures with tailorable topologies. *Chem* **2018**, *4*, 1967-1982.

[36] Lama, S. M.;Pampel, J.;Fellinger, T.-P.;Beškoski, V. P.;Slavković-Beškoski, L.;Antonietti, M.; Molinari, V. Efficiency of Ni nanoparticles supported on hierarchical porous nitrogen-doped

carbon for hydrogenolysis of kraft lignin in flow and batch systems. *ACS Sustainable Chemistry & Engineering* **2017**, *5*, 2415-2420.

[37] Li, M.;Zhu, Y.;Song, N.;Wang, C.; Lu, X. Fabrication of Pt nanoparticles on nitrogen-doped carbon/Ni nanofibers for improved hydrogen evolution activity. *Journal of colloid and interface science* **2018**, *514*, 199-207.

[38] Lu, X. F.;Yu, L.; Lou, X. W. D. Highly crystalline Ni-doped FeP/carbon hollow nanorods as all-pH efficient and durable hydrogen evolving electrocatalysts. *Science advances* **2019**, *5*, eaav6009.

[39] Liang, H.-W.;Brüller, S.;Dong, R.;Zhang, J.;Feng, X.; Müllen, K. Molecular metal–N x centres in porous carbon for electrocatalytic hydrogen evolution. *Nature communications* **2015**, *6*, 7992.

[40] Wu, Z. Y.;Xu, X. X.;Hu, B. C.;Liang, H. W.;Lin, Y.;Chen, L. F.; Yu, S. H. Iron carbide nanoparticles encapsulated in mesoporous Fe-N-doped carbon nanofibers for efficient electrocatalysis. *Angewandte Chemie* **2015**, *127*, 8297-8301.

[41] Su, P.;Iwase, K.;Nakanishi, S.;Hashimoto, K.; Kamiya, K. Nickel-nitrogen-modified graphene: an efficient electrocatalyst for the reduction of carbon dioxide to carbon monoxide. *Small* **2016**, *12*, 6083-6089.

[42] Jin, H.;Wang, J.;Su, D.;Wei, Z.;Pang, Z.; Wang, Y. In situ cobalt–cobalt oxide/N-doped carbon hybrids as superior bifunctional electrocatalysts for hydrogen and oxygen evolution. *Journal of the American Chemical Society* **2015**, *137*, 2688-2694.

[43] Wu, Z.-Y.;Ji, W.-B.;Hu, B.-C.;Liang, H.-W.;Xu, X.-X.;Yu, Z.-L.;Li, B.-Y.; Yu, S.-H. Partially oxidized Ni nanoparticles supported on Ni-N co-doped carbon nanofibers as bifunctional electrocatalysts for overall water splitting. *Nano Energy* **2018**, *51*, 286-293.

[44] Zhang, W.;Zhang, X.;Chen, L.;Dai, J.;Ding, Y.;Ji, L.;Zhao, J.;Yan, M.;Yang, F.; Chang, C.-R. Single-walled carbon nanotube induced optimized electron polarization of rhodium nanocrystals to develop an interface catalyst for highly efficient electrocatalysis. *ACS Catalysis* **2018**, *8*, 8092-8099.

[45] Kresse, G.; Joubert, D. From ultrasoft pseudopotentials to the projector augmented-wave method. *Physical review b* **1999**, *59*, 1758.

[46] Blöchl, P. E. Projector augmented-wave method. *Physical review B* **1994**, *50*, 17953.

[47] Kresse, G.; Furthmüller, J. Efficient iterative schemes for ab initio total-energy calculations

using a plane-wave basis set. *Physical review B* **1996**, *54*, 11169.

[48] Perdew, J. P.;Burke, K.; Ernzerhof, M. Generalized gradient approximation made simple. *Physical review letters* **1996**, *77*, 3865.

[49] Zhang, Y.; Yang, W. Comment on "Generalized gradient approximation made simple". *Physical Review Letters* **1998**, *80*, 890.

[50] Zhu, K. R.;Chen, C. L.;Lu, S. H.;Zhang, X. D.;Alsaedi, A.; Hayat, T. MOFs-induced encapsulation of ultrafine Ni nanoparticles into 3D N-doped graphene-CNT frameworks as a recyclable catalyst for Cr(VI) reduction with formic acid. *Carbon* **2019**, *148*, 52-63.

[51] Lehman, J. H.;Terrones, M.;Mansfield, E.;Hurst, K. E.; Meunier, V. Evaluating the characteristics of multiwall carbon nanotubes. *Carbon* **2011**, *49*, 2581-2602.

[52] Lei, C.;Wang, Y.;Hou, Y.;Liu, P.;Yang, J.;Zhang, T.;Zhuang, X.;Chen, M.;Yang, B.;Lei, L.;Yuan, C.;Qiu, M.; Feng, X. Efficient alkaline hydrogen evolution on atomically dispersed Ni–Nx Species anchored porous carbon with embedded Ni nanoparticles by accelerating water dissociation kinetics. *Energy & Environmental Science* **2019**, *12*, 149-156.

[53] Abbas, S. A.;Iqbal, M. I.;Kim, S.-H.; Jung, K.-D. Catalytic Activity of Urchin-like Ni nanoparticles Prepared by Solvothermal Method for Hydrogen Evolution Reaction in Alkaline Solution. *Electrochimica Acta* **2017**, *227*, 382-390.

[54] Li, R.;Li, X.;Yu, D.;Li, L.;Yang, G.;Zhang, K.;Ramakrishna, S.;Xie, L.; Peng, S. $Ni_3ZnC_{0.7}$ nanodots decorating nitrogen-doped carbon nanotube arrays as a self-standing bifunctional electrocatalyst for water splitting. *Carbon* **2019**, *148*, 496-503.

[55] Min, X.;Sun, B.;Chen, S.;Fang, M.;Wu, X.;Liu, Y. g.;Abdelkader, A.;Huang, Z.;Liu, T.;Xi, K.; Vasant Kumar, R. A textile-based SnO2 ultra-flexible electrode for lithium-ion batteries. *Energy Storage Materials* **2019**, *16*, 597-606.

[56] Fei, H.;Dong, J.;Arellano-Jiménez, M. J.;Ye, G.;Kim, N. D.;Samuel, E. L.;Peng, Z.;Zhu, Z.;Qin, F.; Bao, J. Atomic cobalt on nitrogen-doped graphene for hydrogen generation. *Nature communications* **2015**, *6*, 1-8.

[57] Wang, T.;Sun, Y.;Li, A.;Ma, Y.;Feng, D.;Fang, Y.;Liu, Y.;Huo, Q.;Qiao, Z.-A.; Dai, S. A general synthesis of abundant metal nanoparticles functionalized mesoporous graphitized carbon. *RSC Advances* **2017**, *7*, 50966-50972.

[58] Zhuang, Z.;Giles, S. A.;Zheng, J.;Jenness, G. R.;Caratzoulas, S.;Vlachos, D. G.; Yan, Y. Nickel

supported on nitrogen-doped carbon nanotubes as hydrogen oxidation reaction catalyst in alkaline electrolyte. *Nat Commun* **2016**, *7*, 10141.

[59] Ren, J.;Antonietti, M.; Fellinger, T. P. Efficient water splitting using a simple Ni/N/C paper electrocatalyst. *Advanced Energy Materials* **2015**, *5*, 1401660.

[60] Fan, L.;Liu, P. F.;Yan, X.;Gu, L.;Yang, Z. Z.;Yang, H. G.;Qiu, S.; Yao, X. Atomically isolated nickel species anchored on graphitized carbon for efficient hydrogen evolution electrocatalysis. *Nat Commun* **2016**, *7*, 10667.

[61] Yu, H.;Xue, Y.;Hui, L.;Zhang, C.;Li, Y.;Zuo, Z.;Zhao, Y.;Li, Z.; Li, Y. Efficient Hydrogen Production on a 3D Flexible Heterojunction Material. *Adv Mater* **2018**, *30*, e1707082.

[62] Sun, W.;Du, L.;Du, C.;Gao, Y.; Yin, G. Three-dimensional layered double hydroxides on carbon nanofibers: The engineered mass transfer channels and active sites towards oxygen evolution reaction. *Applied Surface Science* **2019**, *485*, 41-47.

[63] Zhang, W.;Li, Y.;Zeng, X.; Peng, S. Synergetic effect of metal nickel and graphene as a cocatalyst for enhanced photocatalytic hydrogen evolution via dye sensitization. *Scientific Reports* **2015**, *5*.

[64] Wang, J.;Gao, Y.;You, T. L.; Ciucci, F. Bimetal-decorated nanocarbon as a superior electrocatalyst for overall water splitting. *Journal of Power Sources* **2018**, *401*, 312-321.

[65] Dong, T.;Zhang, X.;Wang, P.;Chen, H.-S.; Yang, P. Hierarchical nickel-cobalt phosphide hollow spheres embedded in P-doped reduced graphene oxide towards superior electrochemistry activity. *Carbon* **2019**, *149*, 222-233.

[66] Diaz-Coello, S.;Garcia, G.;Arevalo, M. C.; Pastor, E. Precise determination of Tafel slopes by DEMS. Hydrogen evolution on tungsten-based catalysts in alkaline solution. *International Journal of Hydrogen Energy* **2019**, *44*, 12576-12582.